CrystEngComm

rsc.li/crystengcomm

ROYAL SOCIETY
OF CHEMISTRY
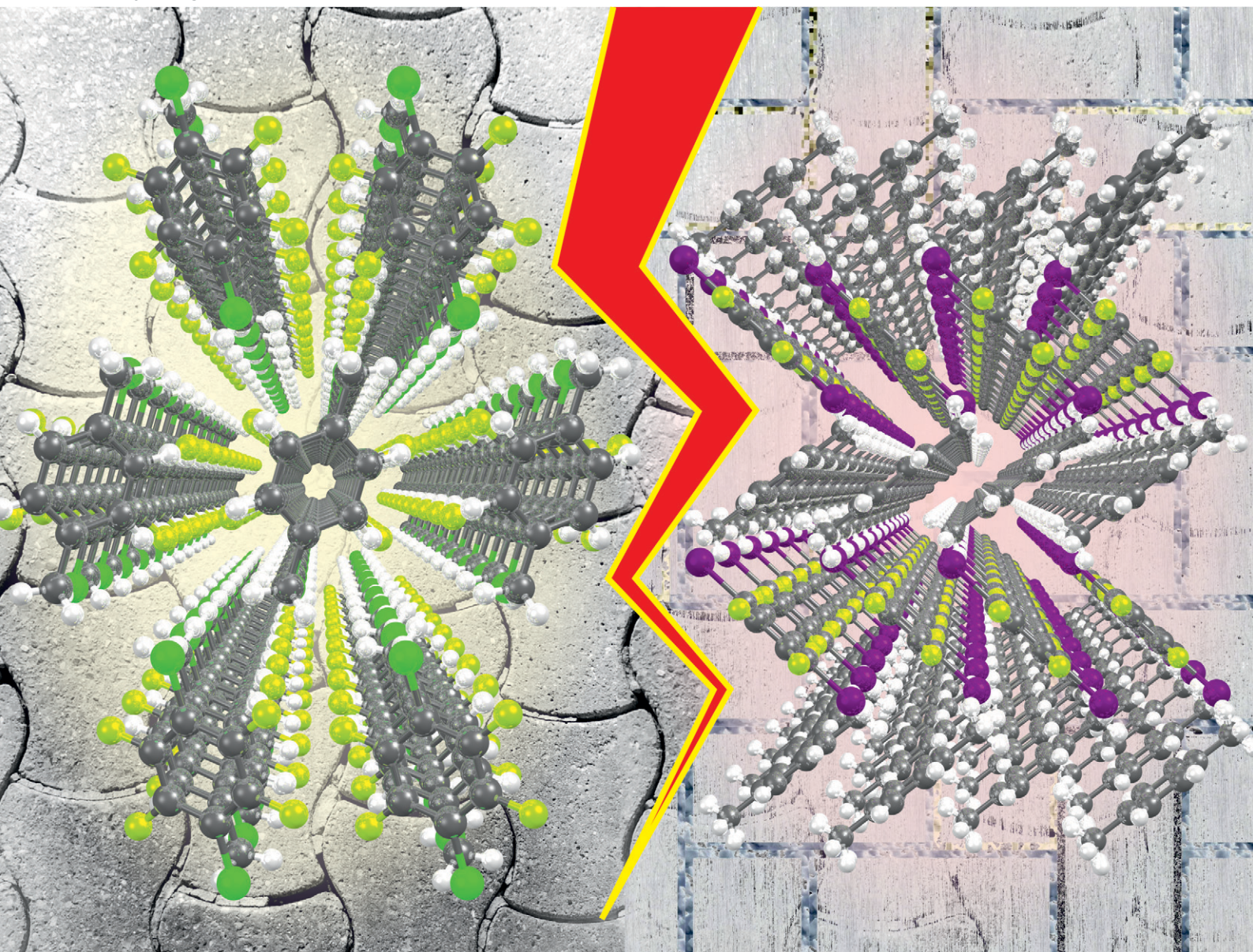
PAPER
Jeremy K. Cockcroft *et. al.*
Exploring non-covalent interactions in binary
aromatic complexes

Check for updates

Exploring non-covalent interactions in binary aromatic complexes†

Joseph C. Bear, [iD] [a] Jeremy K. Cockcroft, [iD] *[b]
Alexander Rosu-Finsen[b] and Jeffrey H. Williams‡

Crystal structure prediction for systems governed by weak non-covalent interactions remain a significant challenge due to the complex energy landscapes involved. Herein, we have experimentally investigated the impact of systematic halogen substitution in fluorinated aromatic co-formers on the formation, structure, and phase behaviour of donor–acceptor adducts and co-crystals with p-xylene (p-$C_6H_4Me_2$). Using a combined approach of differential scanning calorimetry (DSC), variable-temperature powder X-ray diffraction (VT-PXRD), and single-crystal X-ray diffraction (SXD), we have characterized a series of co-crystals formed by p-$C_6H_4Me_2$ with C_6F_5X (X = Cl, Br, I) and p-$C_6F_4X_2$ derivatives. Our results revealed a clear evolution from columnar π-stacked adducts in the Cl-substituted systems to halogen-bonded structures with the heavier halogens (Br, I). The columnar 1:1 adducts exhibit complex solid-state phase behaviour linked to molecular dipole and steric effects, whereas co-crystals involving Br and I show simpler behaviour, with discrete η^2 and η^6 halogen–π interactions both being observed. In one instance, a 1:2 co-crystal was formed with antiferroelectric ordering requiring halogen bonding to p-$C_6H_4Me_2$ from two C_6F_5I molecules. The results underscore the tunability of solid-state architectures through targeted halogen substitution to probe subtle non-covalent interactions. In summary, this work advances our understanding of weak intermolecular forces in crystalline materials and provides data for the predictive design of functional co-crystals.

Introduction

Since the famous quotation by John Maddox[1] in the late 80′s, namely "*one of the continuing scandals in the physical sciences is that it remains in general impossible to predict the structure of even the simplest crystalline solids from a knowledge of their chemical composition*", crystal structure prediction has advanced enormously, as demonstrated for example by the success rate in the series of blind tests[2] organised by the Cambridge Crystallographic Data Centre. The targets used in these blind tests invariably feature molecules with both acceptor and donor groups that can interact strongly. However, when only weak non-covalent interactions are involved, a limitation in structure prediction is the sheer number of similar low-energy solutions in the energy landscape[3] and it is evident that a far greater understanding of weak intermolecular forces in crystalline

materials is required. In addition, interest in non-covalent interactions has been driven by rapid developments in materials science, where weak non-covalent interactions provide a greater, more intricate role in: molecular machines,[4] pharmaceutical drug delivery,[5] battery technologies,[6] and fluorescent/phosphorescent optical materials.[7]

Weak non-covalent (and non-ionic) intermolecular interactions encompass a wide range of intermolecular forces from van der Waals, which are non-directional, to hydrogen-bonding. Other weakly directing forces include: molecular dipoles and higher order electrostatic terms, bond dipoles, and the recently IUPAC-defined halogen bond.[8] Of particular interest for crystal structure prediction are the stacking interactions between aromatic rings, as they are exacting to predict. Originally dubbed "π–π stacking",[9] it is perhaps more intuitive to think of crystal formation in these systems as being directed by the attraction of positive and negative molecular quadrupoles between co-formers, as in the highest temperature rhombohedral phase I of the prototypical system C_6H_6:C_6F_6.[10,11] This special case of face-to-face stacking of aromatic units has also been termed a stacking interaction[12] or an "aromatic donor–acceptor" interaction.[13] However, when C_6H_6:C_6F_6 is cooled to lower temperatures, an increase in the intercolumnar interactions leads to tilting of the rings.[14,15] This

[a] *School of Life Sciences, Pharmacy and Chemistry, Kingston University, Penrhyn Road, Kingston upon Thames KT1 2EE, UK*
[b] *Department of Chemistry, Christopher Ingold Laboratories, University College London, 20 Gordon Street, London WC1H 0AJ, UK. E-mail: j.k.cockcroft@ucl.ac.uk*
† This paper is dedicated to Prof. Judith A. K. Howard CBE FRS on the occasion of her 80th Birthday.
‡ Deceased.

tilting of the rings, often referred to as a so-called "slipped-stacked" arrangement, has been rationalized in terms of competition between London dispersion and Pauli repulsion forces, with electrostatics as an ambivalent spectator.[16] The exchange repulsion energy contribution has a crucial influence on the structure of non-covalently bonded systems.[17]

Derivatives of the parent adduct $C_6H_6 : C_6F_6$ have been studied extensively both experimentally[18–20] and computationally.[21–24] Supplementary experimental studies have attempted to answer the question: *how does changing substituents on the benzene ring affect the non-covalent interaction between molecules and, ultimately, the structures formed?* To that end, our experimental studies on adducts of C_6F_6 with methyl-substituted benzenes, namely: toluene, xylenes, and mesitylene all showed face-to-face stacking of the aromatic units.[19,20] We refer to this arrangement of face-to-face stacking in a 1:1 co-crystal specifically as an *adduct* to distinguish it from other 1:1 co-crystals. Others have studied these derivative systems computationally.[25,26]

However, to date, no in-depth studies involving modifying the C_6F_6 co-former have been made other than two studies from our group.[27,28] We anticipated that substituting one or more of the fluorine atoms with a different halide (X = Cl, Br or I) will have several consequences. Firstly, the quadrupole moment of the co-former can be expected to be reduced as X will less electron withdrawing. Secondly, mono substitution introduces a permanent dipole into the system analogous to that produced by the methyl group in toluene. Thirdly, the substitution of F by a larger halide will reduce the "flatness" of the molecule, especially for Br and I. In a pilot study to this work,[27] simple substitution of a single F for Cl in $C_6H_6 : C_6F_6$ produced an adduct that exhibited similar phases as a function of temperature (and at ambient pressure) to that of both the parent compound and the toluene adduct $C_6H_5Me : C_6F_6$. In a second pilot study, we changed a single F in the C_6F_6 molecule for H and used *p*-xylene (p-$C_6H_4Me_2$) for the co-former.[28]

In this paper, we have investigated the consequences of halide substitution but, in contrast to our first pilot study, we have used p-$C_6H_4Me_2$ as one of the co-formers. The latter is easier to handle and less volatile than benzene, and it has no molecular dipole moment like benzene (in contrast to *e.g.* toluene). In this study, we posed the question: what is the effect of substituting one Cl for F in C_6F_6 on the formation of adducts/co-crystals with p-$C_6H_4Me_2$? Subsequently, on discovering that the structure of the p-$C_6H_4Me_2 : C_6F_5Cl$ adduct exhibits orientational disorder of the C_6F_5Cl moiety, we posed a second question: can C_6F_5Cl be replaced isostructurally in p-$C_6H_4Me_2 : C_6F_5Cl$ with p-$C_6F_4Cl_2$? Finally, we posed a further question: what is the effect of increasing the polarizability (and size) of the X substituent by investigating whether monobromo- and monoiodo-substituted hexafluoro-benzenes formed similar co-crystals?

Experimental

The chemicals: p-$C_6H_4Me_2$ (Sigma-Aldrich, GC grade ≥ 99%), C_6F_5Cl (Sigma-Aldrich, purity 99%), C_6F_5Br (Fluorochem, 99.0%), C_6F_5I (Fluorochem, 99.0%), p-$C_6F_4Cl_2$ (Manchester

Organics, 95%) p-$C_6F_4Br_2$ (Alfa Aesar, 99%), and p-$C_6F_4I_2$ (Fluorochem, 99.0%) were used as received with the exception of p-$C_6F_4Cl_2$. Adducts were prepared as 1:1 molar ratio mixtures of the individual components unless described otherwise. Adducts/co-crystals components were analysed by differential scanning calorimetry (DSC), variable-temperature powder X-ray diffraction (VT-PXRD), and single-crystal X-ray diffraction (SXD) with samples freezing below room temperature using our previously published method.[28] Detailed information on the materials, experimental methods, and instrumentation are provided in the supplementary information (SI).

Results

Co-crystals of p-$C_6H_4Me_2$ with C_6F_5X and p-$C_6F_4X_2$ (X = Cl, Br, and I)

The prototypical adduct formed by benzene and hexafluorobenzene is noted for the formation of a solid at room temperature when the liquid components are added together in a 1:1 molar ratio.[10] However, at room temperature many of the adducts and co-crystals reported here are liquid despite the fact that some of the co-formers are solid at room temperature (see Table 1). Thus, on mixing the components, there is often no visible evidence to suggest adduct or co-crystal formation in the solid phase in contrast to the mixing of benzene and hexafluorobenzene. While the formation of a binary adducts by visual observation of the formation of a solid from liquid components is a useful undergraduate demonstration,[11] the absence of solid formation should not be used to infer that no adduct has formed.

Initial evidence for the formation of a binary adduct or a co-crystal comes from DSC and VT-PXRD measurements. As seen in both DSC and VT-PXRD, all of the adducts/co-crystals in Table 1 exhibit melting points different to that of their constituent components. Furthermore, the observation of different indicative of adduct/co-crystal formation. The ultimate

Table 1 Physical properties of the substances used in this study. Melting points of selected pure substances are from ref. 29; others were obtained in this study. The final column indicates whether a columnar structure was observed (by SXD) in an attempt to form a $C_6H_6 : C_6F_6$ type adduct

Substance	M.W./g mol^{-1}	m.p./K	Liq. at RT?	Adduct?
p-$C_6H_4Me_2$	106.2	286	Y	n/a
C_6F_6	186.1	278	Y	n/a
C_6F_5Cl	202.5	258	Y	n/a
C_6F_5Br	247.0	242	Y	n/a
C_6F_5I	294.0	244	Y	n/a
$C_6F_4Cl_2$	219.0	327	N	n/a
$C_6F_4Br_2$	307.9	354	N	n/a
$C_6F_4I_2$	401.9	383	N	n/a
p-$C_6H_4Me_2 : C_6F_6$	292.3	301	Y	Y
p-$C_6H_4Me_2 : C_6F_5Cl$	308.7	273	Y	Y
p-$C_6H_4Me_2 : C_6F_5Br$	353.2	265	Y	N
$(p$-$C_6H_4Me_2)_{0.5} : C_6F_5I$	347.1	275	Y	N
p-$C_6H_4Me_2 : p$-$C_6F_4Cl_2$	325.2	283	Y	Y
p-$C_6H_4Me_2 : p$-$C_6F_4Br_2$	414.1	352	N	N
p-$C_6H_4Me_2 : p$-$C_6F_4I_2$	508.1	337	n/a	N

proof of adduct *versus* co-crystal formation was obtained by structure determination by SXD.

Adduct of p-C$_6$H$_4$Me$_2$ with C$_6$F$_5$Cl

The DSC data for p-C$_6$H$_4$Me$_2$: C$_6$F$_5$Cl shows two solid-state phases on both cooling and heating (Fig. 1). On cooling, a freezing transition was observed at 273 K and a solid–solid transition was observed at 176 K (ΔH = −1.6 kJ mol^{-1}); on heating, a solid–solid transition was observed at 242 K (ΔH = +1.2 kJ mol^{-1}) with a transition to the melt at 280 K. This solid-state transition shows considerable hysteresis with the I–II transition temperature varying from one run to another. Extra peaks observed at 251 K on cooling, and 268 K on heating, are attributed to a slight excess of C$_6$F$_5$Cl as confirmed in a DSC cycling experiment (Fig. S1). We note that there is a hint of an endothermic peak on heating at 147 K (with an equivalent one on cooling) that is probably due to non-structural changes relating to rotation of the methyl groups in p-C$_6$H$_4$Me$_2$. Similar transitions in this temperature range have been observed previously.[19]

These two solid-state phases were also observed by VT-PXRD using 10 K steps in temperature (Fig. 2 and S2). In addition, VT-PXRD measurements were undertaken in 1 K temperature steps between 250 K and the melt (Fig. S3).

From the PXRD data, lattice parameters and molecular volume were obtained as a function of temperature (see Table S12, Fig. S4a–c and S5). At the I–II phase boundary, there is an abrupt change in volume.

As the I–II phase transition shows considerable hysteresis, care needs to be taken with regard to structure determination by SXD since, as we discovered, it is possible to measure both phases I and II at the *same* temperature (see SI). SXD measurements were made on phase II at 120 K, and on both phases I and II at 200 K.
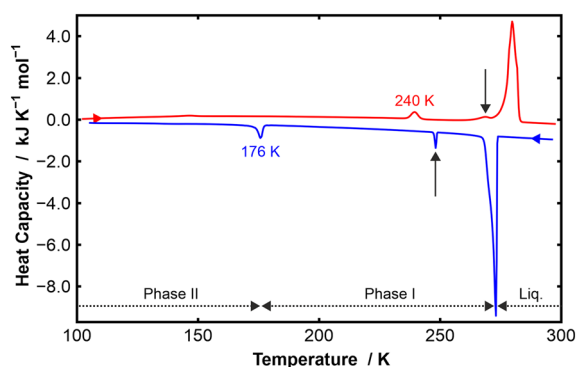

Fig. 2 VT-PXRD data on p-C$_6$H$_4$Me$_2$: C$_6$F$_5$Cl obtained on heating shown as a surface colour plot where the colour scale shows low intensities in the PXRD patterns in blue, intermediate intensities are shown in green/yellow, and high intensities in orange/red. Two solid-state phases are evident. The same raw data is shown as a 3-D plot in Fig. S2.

Adduct of p-C$_6$H$_4$Me$_2$ with p-C$_6$F$_4$Cl$_2$

The DSC data on p-C$_6$H$_4$Me$_2$: p-C$_6$F$_4$Cl$_2$ shows three distinct solid phases on heating (Fig. 3). Solid–solid transitions were observed at 214 K (III → II) and 254 K (II → I) and a transition to the melt at about 283 K. On heating, the III → II transition is exothermic, which is unusual (for this class of materials). However, equivalent transitions are not evident on cooling, but a "sticky" transition is seen starting below around 170 K and extending over about a 40 K range. This sticky transition exhibited similar unusual behaviour to that seen for the protracted phase III to IV transition in C$_6$H$_6$: C$_6$F$_6$.[15]

VT-PXRD on a quench-cooled sample of p-C$_6$H$_4$Me$_2$: p-C$_6$F$_4$Cl$_2$ showed three solid-state phases on heating (Fig. 4 and S7) consistent with the DSC heating curve. The PXRD pattern for phase II has fewer peaks than those observed in

Fig. 1 DSC data (endo up) on a sample of p-C$_6$H$_4$Me$_2$: C$_6$F$_5$Cl showing two solid-state phases. The blue curve was measured on cooling and the red curve on heating. The sample froze at 273 K (ΔH_{freeze} = −20.2 kJ mol^{-1}) and melted at 280 K (ΔH_{fusion} = +20.8 kJ mol^{-1}). The labels to phases II, I, and liquid refer to the temperature ranges in which that phase was stable on *cooling*. The vertical arrows in black show freezing and melting peaks attributed to a slight excess of C$_6$F$_5$Cl. Despite hysteresis, the data is remarkably reproducible (Fig. S1).

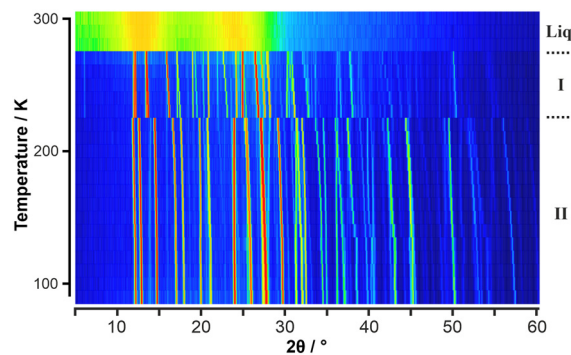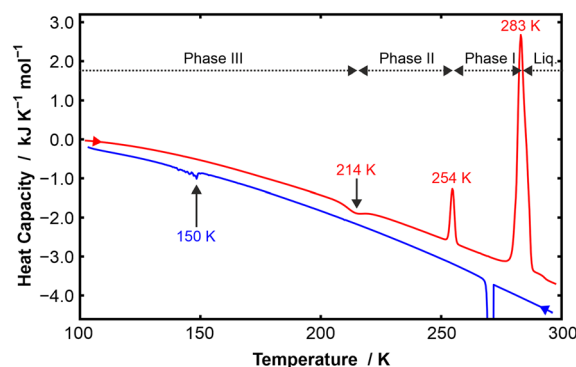**Fig. 3** DSC data (endo up) on a sample of p-C$_6$H$_4$Me$_2$: p-C$_6$F$_4$Cl$_2$ showing three solid-state phases on heating (red curve). The sample melted at 283 K (ΔH_{fusion} = +24.83 kJ mol^{-1}). The labels to phases III, II, I, and liquid refer to the temperature ranges in which that phase was stable on *heating*. However, the blue curve measured on cooling does not show similar phase behaviour as phase I is kinetically stable down to low temperature. At around 150 K on cooling, a series of "sticky" transitions are observed as individual crystallites transform [to phase III]. The reproducibility of the data is demonstrated in Fig. S6.
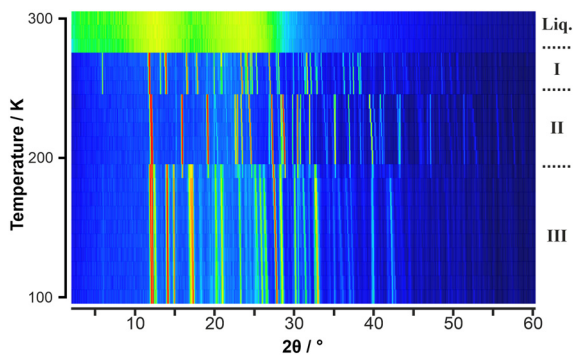
Fig. 4 VT-PXRD data on p-$C_6H_4Me_2$: p-$C_6F_4Cl_2$ obtained on heating shown as a surface colour plot where the colour scale shows low intensities in the PXRD patterns in blue, intermediate intensities are shown in green/yellow, and high intensities in orange/red. Three solid-state phases are evident. The same raw data is shown as a 3-D plot in Fig. S7.

the data for phases I and III, and is missing the low angle peak at about 5.9° seen in these phases. Phase II could be indexed in terms of a monoclinic cell; there is an excellent LeBail fit to the data despite the presence of residual p-$C_6F_4Cl_2$ (Fig. S8). Furthermore, the effect of the sticky transition observed in the DSC was seen in a cooling VT-PXRD experiment in which the sample failed to transform from phase II to III despite being held at 120 K for about 6 hours (Fig. S9).

From the VT-PXRD data, lattice parameters and molecular volume were obtained for phases I and II as a function of temperature (see Table S13, Fig. S10 and S11). Although the volume of phase II of p-$C_6H_4Me_2$: p-$C_6F_4Cl_2$ is slightly smaller than that of phase I, the unusual change of symmetry from triclinic to higher symmetry monoclinic with *decreasing* temperature is indicative of a significant change of structure as seen in the phase III to IV transition of C_6H_6 : C_6F_6.[15,16] This may explain why we were able to determine the structure of phase I from *in situ* crystal growth, but we struggled to obtain SXD data even to solve the structure of phase II.

SXD measurements were made on phase I at 240 K, on phase II at 220 K, and on a new phase, labelled phase IV, at 130 K (see SI). We note that the SXD measurement temperature for phase I is below the II–I transition temperature (254 K) seen on heating in DSC, but this is possible due to the stability of phase I at this temperature as a result of hysteresis. The calculated PXRD pattern of phase IV (Fig. S12) surprisingly was *not* a match to the observed PXRD data of phase III, which could not be indexed. However, we were unable to obtain analysable SXD data on phase III despite repeated attempts. With regard to the measurement temperatures, the authors note that the DSC data was not very informative in this instance as the SXD measurements were made on cooling.

Co-crystal of p-$C_6H_4Me_2$ with C_6F_5X (X = Br or I)

DSC data on 1 : 1 molar mixture of p-$C_6H_4Me_2$ with C_6F_5Br showed no solid-state phase transitions (Fig. S13). The

structure of p-$C_6H_4Me_2$: C_6F_5Br at 120 K was determined by SXD as a 1 : 1 adduct. VT-PXRD data on this co-crystal showed no evidence for solid-state phase transitions (Fig. S14), and was consistent with the SXD data. From the PXRD data, lattice parameters and molecular volume were obtained as a function of temperature (Table S14, Fig. S15 and S16). However, cooling a 1 : 1 molar mixture of p-$C_6H_4Me_2$ and C_6F_5I to 120 K led to the growth of a crystal in which the molar ratio of p-$C_6H_4Me_2$ and C_6F_5I components was shown to be 1 : 2 by SXD. This was consistent with DSC results using a sample prepared unwittingly in a 1 : 1 molar ratio (Fig. S17), which exhibited complex melting behaviour due to the sample being a 1 : 1 molar mixture of $C_6H_4Me_2$: $(C_6F_5I)_2$ and excess $C_6H_4Me_2$. Subsequent VT-PXRD measurements were made on a mixture of p-$C_6H_4Me_2$ and C_6F_5I in a 1 : 2 molar ratio. As for p-$C_6H_4Me_2$: C_6F_5Br, no solid-state phase transitions for p-$C_6H_4Me_2$: $(C_6F_5I)_2$ were observed (Fig. S18). Lattice parameters obtained from PXRD data on the sample at 120 K (Table S15) matched those from the SXD measurement.

Co-crystal of p-$C_6H_4Me_2$ with p-$C_6F_4X_2$ (X = Br or I)

Low-temperature DSC data on 1 : 1 molar mixtures of p-$C_6H_4Me_2$ with p-$C_6F_4Br_2$ and p-$C_6F_4I_2$ showed no evidence for solid-state phase transitions (Fig. S19 and S20). The solid-state structures of p-$C_6H_4Me_2$: p-$C_6F_4Br_2$ and p-$C_6H_4Me_2$: p-$C_6F_4I_2$ were determined from SXD. The unit cells determined by SXD matched those determined from the room temperature PXRD data (Fig. S21). As they were not columnar adducts, and as they exhibited no phase transitions, these co-crystals were not investigated further by VT-PXRD.

A summary of all SXD results reported in this paper are given in Table 2.

Discussion

Previously, our investigations focussed on perturbing the non-covalent interactions in the prototypical adduct C_6H_6 : C_6F_6 by either substitution of –H by –CH_3 in the benzene ring or by substitution of –F by –Cl or –H in hexafluorobenzene.[21,27,28] There are a number of advantages in expanding our studies with the use of p-xylene (p-$C_6H_4Me_2$) with substituted hexafluorobenzenes. Like C_6H_6, p-$C_6H_4Me_2$ has no dipole moment. Secondly, it is easier to handle due to its lower volatility. Thirdly, it was noticed that p-$C_6H_4Me_2$ formed more solid adducts than C_6H_6 with different co-formers at room temperature. Solid adducts are easier to analyse *via* SXD as the crystallographer can select and mount a single crystal manually. However, recent work by our group on multi-grain crystallographic methods allows for the analysis of multiple single crystals in the beam grown *in situ* from the melt whilst mounted on the diffractometer.[28] Thus, we were able to largely overcome this limitation and analyse mixtures, which are liquid at room temperature. The combination of low temperature DSC and VT-PXRD allows for the rapid identification of phase transitions, and thus suggest temperatures at which SXD

Table 2 Unit cell parameters for the single-crystal structures reported in this paper. Entries with a single solid-state phase are denoted with an asterisk ("*"). Entries with a "‡" denote structures of p-C₆H₄Me₂:C₆F₆ measured in our previous studies[21] but with a different choice of unit cell in order to aid comparison with new structures in this work

Sample	Phase	T/K	S.G.	Z	a/Å	b/Å	c/Å	α/°	β/°	γ/°	V/Z/Å³
p-C₆H₄Me₂:C₆F₆‡	II	240	$P\bar{1}$	1	6.4824(5)	7.2938(6)	7.5328(5)	105.295(7)	101.979(6)	96.465(7)	330.74(5)
p-C₆H₄Me₂:C₆F₆‡	III	150	$P\bar{1}$	1	6.1308(4)	7.2896(5)	7.7362(4)	107.632(5)	101.940(5)	95.058(5)	318.12(4)
p-C₆H₄Me₂:C₆F₅Cl	I	200	$P\bar{1}$	2	6.5505(4)	7.3190(4)	14.6880(8)	89.116(4)	102.483(5)	94.488(5)	342.72(4)
p-C₆H₄Me₂:C₆F₅Cl	II	200	$P\bar{1}$	1	6.2099(4)	7.4687(4)	7.9874(4)	109.801(5)	99.549(5)	95.567(5)	339.00(3)
p-C₆H₄Me₂:C₆F₅Cl	II	120	$P\bar{1}$	1	6.1383(5)	7.4411(7)	7.9224(6)	111.378(8)	99.662(7)	95.159(7)	327.65(5)
p-C₆H₄Me₂:p-C₆F₄Cl₂	I	240	$P\bar{1}$	2	6.4620(4)	7.4574(4)	15.1315(7)	90.380(4)	100.429(5)	94.132(5)	357.57(4)
p-C₆H₄Me₂:p-C₆F₄Cl₂	II	220	$P2_1/n11$	2	5.98846(7)	7.90133(9)	14.83490(17)	96.4603(10)	90	90	348.742(7)
p-C₆H₄Me₂:p-C₆F₄Cl₂	IV	130	$P\bar{1}$	1	6.3455(3)	7.5012(3)	7.7599(3)	109.370(4)	98.590(4)	90.299(3)	343.95(3)
p-C₆H₄Me₂:C₆F₅Br	*	120	$P12_1/n1$	4	9.0813(3)	15.2000(5)	9.8653(2)	90	99.229(2)	90	336.11(2)
p-C₆H₄Me₂:p-C₆F₄Br₂	*	150	$C12/m1$	2	8.4576(3)	8.3594(3)	9.8748(3)	90	92.357(3)	90	348.78(2)
p-C₆H₄Me₂:(C₆F₅I)₂	*	120	$P\bar{1}$	1	6.04191(17)	8.9855(2)	9.9891(3)	74.629(2)	89.584(2)	89.675(2)	522.89(2)
p-C₆H₄Me₂:p-C₆F₄I₂	*	150	$C12/m1$	2	8.5140(7)	8.5541(8)	10.2442(8)	90	93.450(7)	90	372.37(6)

experiments should be undertaken. In this way, we stood the best possible chance that the crystals would not undergo any phase transitions during SXD data acquisition.

The following discussion section follows the same sequence as the results section, allowing the reader to match the results from one system with the corresponding discussion.

The pure components

The solid-state structure of p-xylene has previously been well characterised.[30] By contrast, until recently, the chlorine- and bromo-substituted fluorobenzenes used in this study had not been thoroughly characterised in solid form. As this essential data was missing, our group investigated the solid-state behaviour of C₆F₅Cl and C₆F₅Br, as well as p-C₆F₄Cl₂ as a forerunner to our current work.[31,32]

The structures of phases II and III of C₆F₅Cl were solved from SXD data obtained *in situ* from the sample at 200 K and 150 K, respectively. An additional transient phase was observed just below the melt, labelled as phase I but we were unable to determine its structure. Additionally, the crystal structure of p-C₆F₄Cl₂ was determined by SXD at 150 K.[31]

The complex phase behaviour of C₆F₅Br has been reported by us recently[32] whilst the structure of the p-C₆F₄Br₂ has previously been determined.[33–35] Likewise, the crystal structures of C₆F₅I and p-C₆F₄I₂ have previously been determined by others.[35–39]

Adduct of p-C₆H₄Me₂ with C₆F₆

In our previous work, we showed that a 1:1 molar mixture of p-C₆H₄Me₂ and C₆F₆ forms a columnar adduct with three solid-state phases.[21] In the lowest temperature phase III, the molecules align such that the C–CH₃ bonds in p-xylene are co-linear with the C–F bonds in C₆F₆ resulting in an eclipsed conformation (Fig. 5). On increasing the temperature, the bond dipole interaction between the C–CH₃ and C–F bonds weakens leading to the formation of phase II in which the molecules now exhibit a staggered conformation (Fig. 6). Above 246 K, increased librational motion of the p-xylene molecules leads to the formation of monoclinic phase I in which the molecules

exhibit mirror and twofold symmetry. On cooling back to the triclinic phase II, the molecules are in a position of unstable equilibrium with respect to mirror and twofold symmetry and these symmetry elements are therefore lost.

Adduct of p-C₆H₄Me₂ with C₆F₅Cl

In this work, we investigated the effect of substitution of a single fluorine atom in C₆F₆ by a chlorine atom with respect to adduct formation and its properties as a function of temperature. A 1:1 molar mixture of p-C₆H₄Me₂ and C₆F₅Cl forms a columnar adduct but this adduct only exhibits two solid-state phases as seen by DSC and VT-PXRD (Fig. 1 and 2). In the lowest temperature phase II, the molecules align such that the C–CH₃ bonds in p-xylene are co-linear with the C–Cl bond in C₆F₅Cl resulting in an eclipsed conformation (Fig. 5), similar to the behaviour observed for phase III of p-C₆H₄Me₂:C₆F₆. In both p-C₆H₄Me₂:C₆F₆ and p-C₆H₄Me₂:C₆F₅Cl, the molecules are centred on the inversion points with space group $P\bar{1}$, necessitating disorder of the C₆F₅Cl molecule over two opposite orientations in equal measure, *i.e.* 50:50 percentage site occupation of Cl (for a F atom) across the two symmetry-related positions.

In its higher temperature phase, C₆H₄Me₂:C₆F₅Cl (I) exhibits a staggered conformation in the triclinic space group $P\bar{1}$. However, in contrast to phase II, the molecules are no longer centred on symmetry inversion points. Consequently, the disorder is no longer constrained to be 50:50 percentage by symmetry, and the refined orientational disorder for the two positions is 38:62 percentage site occupation. The lack of molecular inversion symmetry results in twice the number of molecules per unit cell as evidenced by the cell doubling seen in the VT-PXRD experiment (Fig. 2). A transition leading to the doubling of the unit cell but with no change in space-group symmetry on heating is unusual.

The phase II to phase I transition appears to be driven by the combination of molecules moving from eclipsed to staggered plus a lateral movement of the molecules leading to a slipped-disc columnar structure. As seen in Fig. 6, the formation of a slipped-disc structure with staggered conformation of the
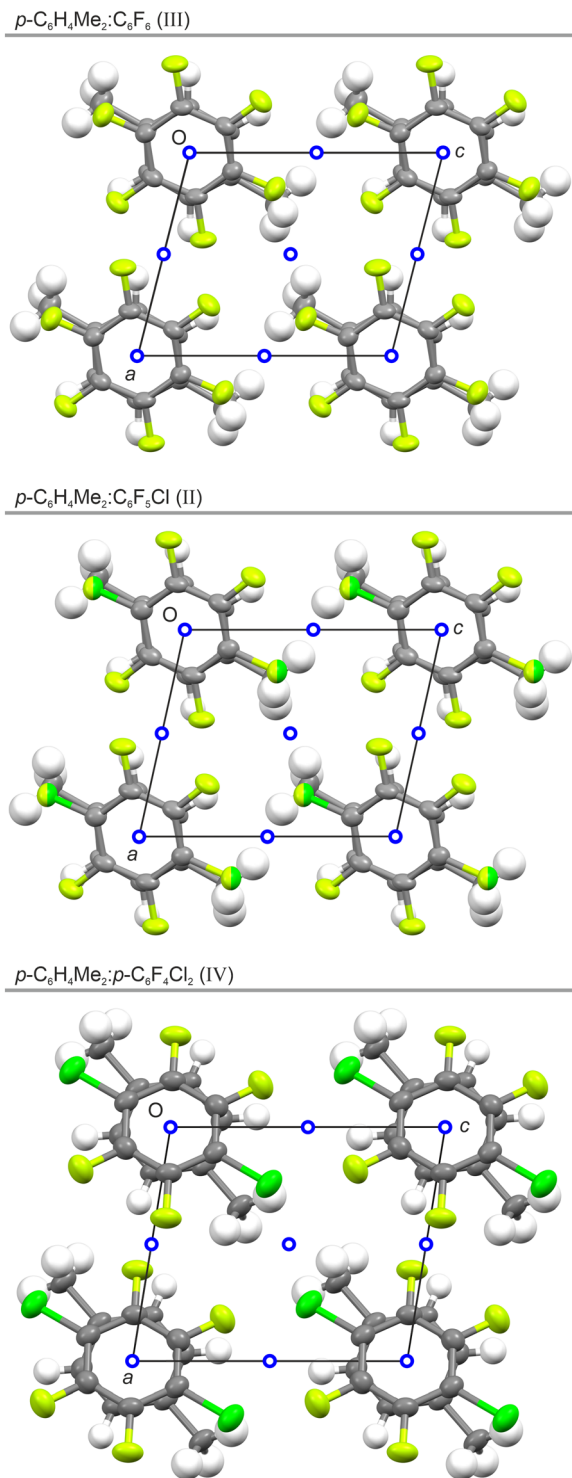
p-$C_6H_4Me_2$:C_6F_6 (III)

p-$C_6H_4Me_2$:C_6F_5Cl (II)

p-$C_6H_4Me_2$:p-$C_6F_4Cl_2$ (IV)

Fig. 5 Comparison of the crystal structures of the adducts formed by p-$C_6H_4Me_2$ with C_6F_6 at 150 K in phase III (top), with C_6F_5Cl at 120 K in phase II (middle), and with p-$C_6F_4Cl_2$ at 130 K in phase IV (bottom), all viewed along **b** showing that the co-formers in each structure lie on symmetry inversion points (blue open circles) and that the molecules adopt either eclipsed or semi-eclipsed positions in each structure. Due to presence of the inversion centres, the C_6F_5Cl molecules in p-$C_6H_4Me_2$:C_6F_5Cl exhibit orientational disorder with respect to the direction of the C–Cl bond, which is in near co-parallel alignment with the C–CH_3 bond of the p-$C_6H_4Me_2$ moiety.

molecules for phase I of $C_6H_4Me_2$:C_6F_5Cl is in contrast to the behaviour seen in phases II and III of p-$C_6H_4Me_2$:C_6F_6, in which the molecules are staggered but remain aligned along the column axis.

This major structural change in going between phases I and II of p-$C_6H_4Me_2$:C_6F_5Cl is reflected in the DSC measurement where significant hysteresis is observed (Fig. 1). This large hysteresis enabled us to measure both phase I and phase II at the same temperature (200 K) in an SXD experiment! The observation of a monoclinic phase in p-$C_6H_4Me_2$:C_6F_6 raised the question of the existence of a third solid-state phase existing just below the melt in p-$C_6H_4Me_2$:C_6F_5Cl. VT-PXRD in very fine (1 K) steps (Fig. S3) showed no evidence for an additional phase in contrast to the observation of a monoclinic phase just below the melt in p-$C_6H_4Me_2$:C_6F_6.[21]

Adduct of p-$C_6H_4Me_2$ with p-$C_6F_4Cl_2$

The observation of a structure with either roughly 50% (phase I) or exactly 50% (phase II) orientational disorder of the C_6F_5Cl molecules in p-$C_6H_4Me_2$:C_6F_5Cl raised the question of whether an isomorphous structure would be formed when C_6F_5Cl is substituted with p-$C_6F_4Cl_2$. Hence, we subsequently investigated the effect of substitution of C_6F_5Cl with p-$C_6F_4Cl_2$ with regard to adduct formation and the properties of any adduct as a function of temperature. Our experiments showed that a 1:1 molar mixture of p-$C_6H_4Me_2$ and p-$C_6F_4Cl_2$ forms a columnar adduct, but that this adduct exhibits at least *three* solid-state phases (Fig. 4 and 5). The crystal structures of phases I, II, and IV are illustrated in Fig. 6, 7, and 5, respectively; however, we were unable to determine the structure of phase III observed in the PXRD measurements.

The highest-temperature phase I of p-$C_6H_4Me_2$:p-$C_6F_4Cl_2$ exhibits a staggered conformation in the triclinic space-group $P\bar{1}$, the structure being isomorphous to that of $C_6H_4Me_2$:C_6F_5Cl (I) demonstrating that C_6F_5Cl *can* be replaced by p-$C_6F_4Cl_2$. As with $C_6H_4Me_2$:C_6F_5Cl (I), p-$C_6H_4Me_2$:p-$C_6F_4Cl_2$ (I) exhibits a slipped-disc column arrangement with two different centroid-to-centroid distances. The lattice parameters for both adducts are broadly similar (Table 2) and differ mainly due to the different measurement temperatures employed (200 K *vs.* 240 K), the latter chosen in light of the phase transitions observed in these two adducts.

Although the monoclinic cell parameters of phase II of p-$C_6H_4Me_2$:p-$C_6F_4Cl_2$ in space-group $P2_1/n11$ are broadly similar to those of phase I, the structures are quite different. Firstly, the columns of molecules in phase II are approximately close-packed leading to a significant reduction in volume per molecule (Table 2). Secondly, the molecules within a column do not exhibit a slipped-disc column arrangement as in phase I, but are instead eclipsed where the methyl groups of p-$C_6H_4Me_2$ are superimposed upon the chlorine atoms of the p-$C_6F_4Cl_2$. Finally, the molecules in one column are tilted at an opposite angle to those in a neighbouring column (Fig. 7). The tilting of the rings avoids direct face-to-face stacking of the electron dense π-clouds of the aromatic rings, which is a repulsive
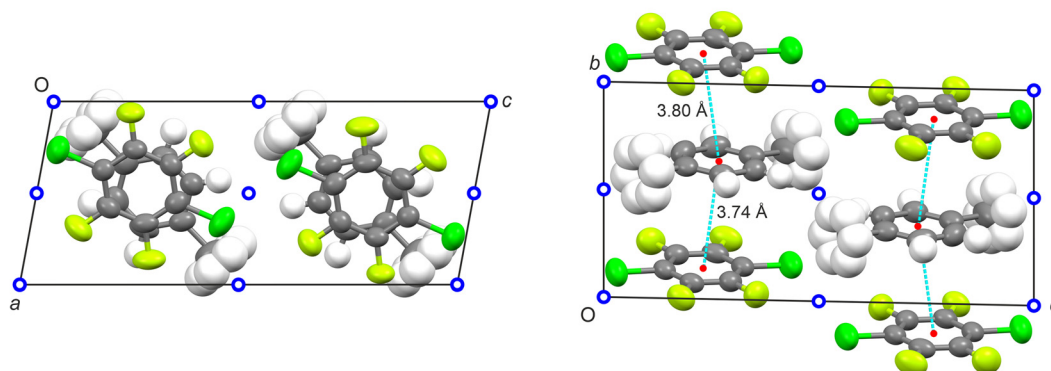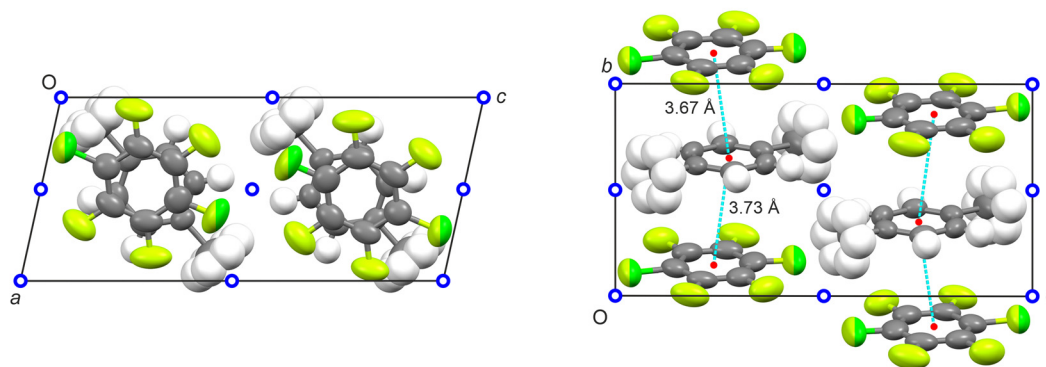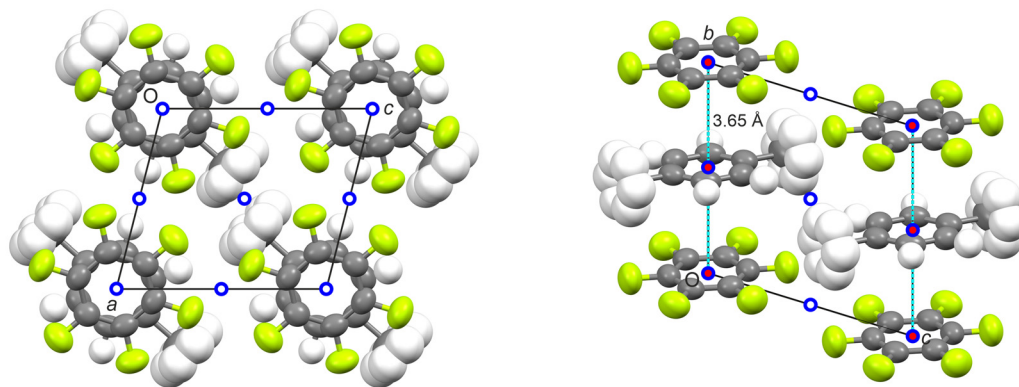
Fig. 6 Comparison of the triclinic crystal structures of phase II of the p-C$_6$H$_4$Me$_2$ and C$_6$F$_6$ adduct at 240 K (top), phase I of the p-C$_6$H$_4$Me$_2$ and C$_6$F$_5$Cl adduct at 200 K (middle), and phase I of the p-C$_6$H$_4$Me$_2$ and p-C$_6$F$_4$Cl$_2$ adduct at 240 K (bottom) viewed along **b** (left) and viewed along **a** (right) showing that the co-formers in each of these structures exhibit staggered conformations. The C$_6$F$_5$Cl molecules in p-C$_6$H$_4$Me$_2$: C$_6$F$_5$Cl (I) exhibit orientational disorder with respect to the direction of the C–Cl bond, which is not parallel to the C–CH$_3$ bond of the p-C$_6$H$_4$Me$_2$ moiety. The blue open circles show the inversion symmetry points in each structure. It can be seen that the inversion point is within the molecules for p-C$_6$H$_4$Me$_2$: C$_6$F$_6$ but between molecules in both p-C$_6$H$_4$Me$_2$: C$_6$F$_5$Cl and p-C$_6$H$_4$Me$_2$: p-C$_6$F$_4$Cl$_2$ leading to a slipped disc column arrangement in these isostructural adducts. The centroids of the discs are marked with a filled red circle.

interaction. Given the observed tilts, this is evidently stronger than the competing quadrupole attraction between molecules, which by itself would favour face-to-face stacking.

The powder diffraction patterns of "phase III" of p-C$_6$H$_4$Me$_2$: p-C$_6$F$_4$Cl$_2$ could not be indexed. Repeat measurements suggested that the solid produced by quenching might be a mixture of two phases. Attempts to produce phase III by slow cooling of the sample resulted solely in the observation of phase II (down to

120 K). In the absence of a crystal structure solution, one might speculate that the structure of phase III might have similar packing to phase II but with either a staggered arrangement of the rings (as seen in related materials at low temperature) or with a change to the relative tilts of the molecules within a column. However, in the SXD experiments, cooling the sample of p-C$_6$H$_4$Me$_2$: p-C$_6$F$_4$Cl$_2$ in phase II resulted in at least one large crystal of "phase IV" being formed, whose calculated PXRD
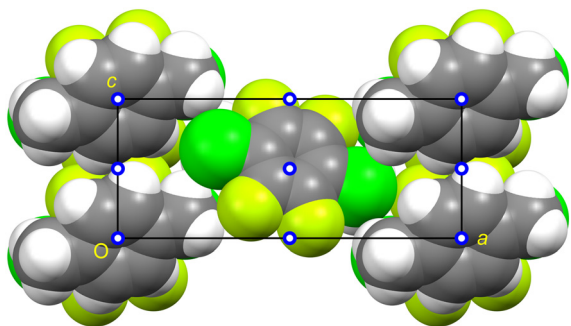
Fig. 7 Phase II of p-$C_6H_4Me_2$:p-$C_6F_4Cl_2$ seen down the b-axis at 220 K showing the eclipsed configuration (in contrast to phase I) of the methyl and chlorine atoms on the aromatic rings and the tilt of the rings with respect to the molecular column axis. All molecules lie on points of inversion (shown as open blue circles) despite the optical off-centre illusion! The structure was refined (and submitted to CCDC) in the monoclinic space group $P112_1/n$ (*i.e.* with z-axis unique) instead of the ideal x-axis unique setting ($P2_1/n11$, as used for the VT-PXRD analysis to aid comparison with phase I) due to software bugs in data processing and validation tools when using non-standard settings of monoclinic space groups.
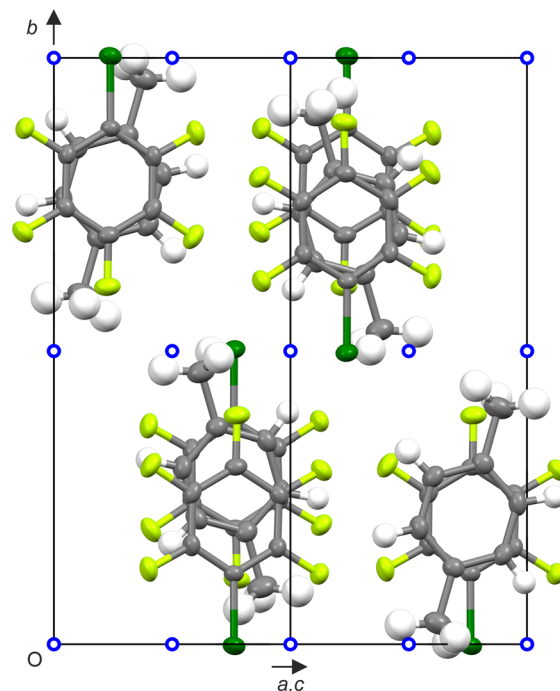
Fig. 8 Crystal structure of p-$C_6H_4Me_2$:C_6F_5Br at 120 K viewed perpendicular to b and down the columns of molecules, with C atoms shown in grey, H atoms in white, F atoms in light green, and Br atoms in dark-green. Open blue circles show the position of inversion centres within the structure, which are always between molecule, thus leading to antiferroelectric ordering of the C_6F_5Br molecular dipole along a column axis as well as between columns.

pattern differed to that of phase III (see Fig. S12). Phase IV has a larger volume than super-cooled phase II (Fig. S11), suggesting it to be a metastable phase.

As shown in Fig. 5, the structure of p-$C_6H_4Me_2$:p-$C_6F_4Cl_2$ (IV) exhibits a semi-eclipsed conformation similar to that seen in p-$C_6H_4Me_2$:C_6F_6 (III) and p-$C_6H_4Me_2$:C_6F_5Cl (II). As for the other two adducts at low temperature, we speculate that p-$C_6H_4Me_2$:p-$C_6F_4Cl_2$ (IV) is the most thermodynamically stable phase. As for phase II, but in contrast to phase I, there is an equal distance between the centroids of the p-$C_6H_4Me_2$ and p-$C_6F_4Cl_2$ rings along the column axis.

It is interesting to note in each of p-$C_6H_4Me_2$:C_6F_6, p-$C_6H_4Me_2$:C_6F_5Cl, and p-$C_6H_4Me_2$:p-$C_6F_4Cl_2$ that staggered conformations between co-formers are seen at the higher temperatures. On lowering the temperature, an eclipsed conformation is preferred, though for p-$C_6H_4Me_2$:p-$C_6F_4Cl_2$ a perfectly eclipsed conformation is not achieved. There is competition between the alignment of C–Me with C–Cl bond dipoles and C–H with C–F bond dipoles and steric repulsion due to the presence of larger halides on the substituted C_6F_6 ring, leading to this imperfectly eclipsed conformation.

Co-crystals of p-$C_6H_4Me_2$ with C_6F_5X (X = Br or I)

The mono-halogen-substituted C_6F_5X co-formers, namely C_6F_5Cl, C_6F_5Br, and C_6F_5I have a molecular dipole that increases in going from Cl through to I. The effect of this is seen in the co-crystals formed. The single phase observed for p-$C_6H_4Me_2$:C_6F_5Br has a slipped-disc columnar adduct similar to phase I of p-$C_6H_4Me_2$:C_6F_5Cl, but with antiferroelectric ordering of the molecular dipole (Fig. 8 and S22). The discs are slipped to a larger extent in the bromo co-crystal presumably to accommodate the larger size of the Br atom. In addition, the steric effect of the Br atoms leads to only partial alignment of

the C–Me and C–Br bond dipoles and an imperfectly eclipsed conformation.

By contrast, the interaction of p-$C_6H_4Me_2$ and C_6F_5I does not cause the formation of a columnar adduct as the non-covalent interactions are driven by halogen bonding tending towards an "η_2" type halogen bond interaction (based on closest C–X distances) with the aromatic ring of p-$C_6H_4Me_2$ (Fig. 9 and S23). As shown by Wong *et al.*[39] *via* a CCDC database study combined with DFT calculations, "η_1" interactions (where the halogen points towards a single carbon atom) and "η_2" (where the halogen points towards the C–C aromatic bond) dominate CCDC database entries of π-type halogen bonds and this is what we observe here. The increase in the molecular dipole moment in C_6F_5X in going from F to I favours antiferroelectric ordering of the C_6F_5X molecules. In addition, the larger size of I strongly discourages columnar adduct formation on steric grounds. The stronger antiferroelectric interactions in p-$C_6H_4Me_2$:$(C_6F_5I)_2$ (and also in p-$C_6H_4Me_2$:C_6F_5Br) probably results in the absence of phase transitions to disordered phases on heating (as shown by DSC or VT-PXRD) in contrast to the behaviour shown, for example, by p-$C_6H_4Me_2$:C_6F_5Cl, or indeed by the parent co-crystal p-$C_6H_4Me_2$:C_6F_6.

The co-crystal of p-$C_6H_4Me_2$ and C_6F_5I is formed in a 1:2 ratio as found in previous work on C_6H_6:$(C_6F_5I)_2$.[36] This enables halogen bonding to form on both sides of the aromatic ring of p-$C_6H_4Me_2$ (Fig. S23). By contrast, we note that the co-
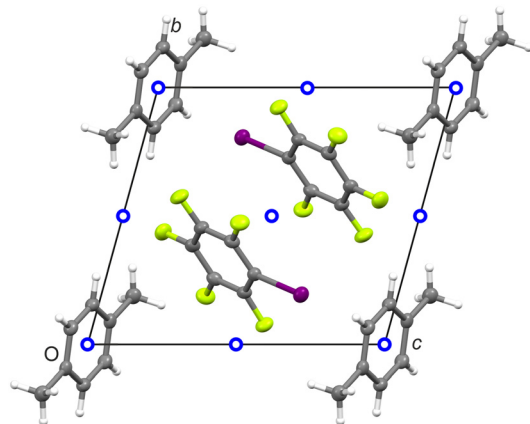
Fig. 9 Crystal structure of p-$C_6H_4Me_2$: C_6F_5I seen down the a-axis at 120 K, with C atoms shown in grey, H atoms in white, F atoms in light green, and I atoms in purple. Open blue circles show the position of inversion centres within the structure, which lie at the centres of the p-$C_6H_4Me_2$ molecules, but are between the C_6F_5I molecules leading to an antiferroelectric arrangement.

Fig. 10 Non-covalent interactions between p-$C_6H_4Me_2$ and p-$C_6F_4Br_2$ with the less common η_6 halogen bond (based on similar C–X distances) represented by a dashed line in cyan between the centre of the C_6-ring (shown by an open blue circle at the point of inversion symmetry) and the bromine atom; C atoms are shown in grey, H atoms in white, F atoms in light green, and Br atoms in dark green. The six Br to C distances (of the C_6 ring in p-$C_6H_4Me_2$) are equal to 3.670 Å (×2), 3.671 Å (×2), 3.681 Å, and 3.683 Å. Atoms are shown at 50% probability except for H which is shown at a fixed radius of 0.2 Å.

crystal C_6H_6 : $(C_6F_5I)_2$ has both high- and low-temperature phases, but in each form, the iodine atoms are found in layers with the C_6H_6 molecules sandwiched between two C_6F_5I molecules. Thus, despite the same compositional ratios, the crystal structures of p-$C_6H_4Me_2$: $(C_6F_5I)_2$ and C_6H_6 : $(C_6F_5I)_2$ (in either phase) are not related demonstrating the effects of different competing non-covalent interactions.

Co-crystals of p-$C_6H_4Me_2$ with p-$C_6F_4X_2$ (X = Br or I)

The co-formers C_6F_6, p-$C_6F_4Cl_2$, p-$C_6F_4Br_2$, and p-$C_6F_4I_2$ have no molecular dipole. In addition, the quadrupole moment of the molecules is expected to decrease in going from C_6F_6 through to p-$C_6F_4I_2$. A consequence of this is that columnar adduct formation is expected to become less favourable, but halogen bond formation is expected to become more favourable for crystal growth.

Initially, we posed the question as to whether a columnar adduct could be formed between p-$C_6H_4Me_2$ and p-$C_6F_4Br_2$, given that one forms between p-$C_6H_4Me_2$ and C_6F_5Br. In contrast to the crystal structures formed by p-$C_6H_4Me_2$: p-$C_6F_4Cl_2$, SXD showed that the structure formed by p-$C_6H_4Me_2$: p-$C_6F_4Br_2$ is not a columnar adduct, but a 1 : 1 co-crystal structure dominated by the less common η_6 halogen bonding (Fig. 10), where the halogen atom is roughly equidistant from the six carbons of the aromatic ring, which is usually less favoured as the lone pair of the halogen experiences strong repulsion from the π-cloud.[39] The molecules are arranged in a herringbone motif (Fig. S24).

Likewise, the crystal structure formed by p-$C_6F_4I_2$ dissolved in an excess of p-$C_6H_4Me_2$ also leads to the formation of a 1 : 1 co-crystal, which is isostructural to p-$C_6H_4Me_2$: p-$C_6F_4Br_2$ (Fig. S25). The halogen bond in p-$C_6H_4Me_2$: p-$C_6F_4I_2$ still tends towards η_6 but is less symmetric, leaning towards η_1 type

behaviour (with C⋯I varying from 3.64 Å to 3.76 Å), with the distance to the centroid of the p-$C_6H_4Me_2$ ring being 3.43 Å.

As an aside, we note that a co-crystal structure of C_6H_6 and p-$C_6F_4I_2$ has been reported with triclinic symmetry.[40] However, our measurements on C_6H_6 : p-$C_6F_4I_2$ showed that its crystal structure has the same monoclinic space-group symmetry ($C2/m$) as exhibited by p-$C_6H_4Me_2$: p-$C_6F_4X_2$ for X = Br and I, but it is not isostructural (Fig. S26). In the crystal structure of C_6H_6 : p-$C_6F_4I_2$, halogen bonding is via the more common η_2 type interaction.

It is interesting to contrast the structures formed by p-$C_6F_4Br_2$ with p-$C_6H_4Me_2$ and those stacked structures formed by p-$C_6F_4Br_2$ with larger aromatics. A search of the Cambridge Structural Database reveals the following columnar adducts with aromatic hydrocarbons: phenanthrene (REVQAM),[41] fluoranthene (NEHDOW),[42] triphenylene (RINPEM),[33] and pyrene (GUQRAN);[7] all of which exhibit columnar structures. These structures indicate that there is seemingly a fine balance between the various structure-directing non-covalent interactions, namely quadrupole and bond-dipole moments versus halogen-bonds. This suggests that the different structural type formed by p-$C_6H_4Me_2$: p-$C_6F_4Br_2$ is a result of differences in the magnitude of these forces. It is noteworthy that a similar search of the Cambridge Structural Database revealed fewer columnar adducts between p-$C_6F_4I_2$ and aromatic hydrocarbons. Thus a columnar adduct is formed with triphenylene (RINPOW)[33] and pyrene (FARNOD);[43] but not with fluoranthene (NEHCIP)[42] or phenanthrene (NICSUP).[44] This may be due to the greater tendency of iodinated aromatics to form halogen bonds in co-crystals with aromatic hydrocarbons.[45]

Conclusions

In this paper, we have investigated the consequences of mono- and p-di-halide substitution in C_6F_6 on the formation of adducts/co-crystals with p-$C_6H_4Me_2$. The resulting stable adducts/co-crystals and their phase behaviour as a function of temperature have been characterised by a combination of DSC, VT-PXRD, and SXD. With p-$C_6H_4Me_2$, C_6F_5Cl, p-$C_6F_4Cl_2$, and C_6F_5Br formed columnar adducts whereas p-$C_6F_4Br_2$, C_6F_5I, and

p-$C_6F_4I_2$ formed co-crystals with halogen bonding. The columnar adducts exhibited complex phase behaviour, often with several phase transitions up to the melt, whereas simple co-crystals exhibited a single solid phase down to 100 K.

The difference between the two groups can be attributed to the change in the relative strengths of the different types of non-covalent interaction in these materials. When substituting F (in C_6F_6) with Cl, Br, and then I, the propensity for halogen bonding can be expected to increase; conversely, the quadrupole moment, which is thought to direct alignment of the molecules in columns (from the liquid phase), is expected to decrease. Although p-di-substituted C_6F_6 derivatives have no molecular dipole, the mono-substituted forms possess a molecular dipole whose strength is expected to increase in going from F down to I.

The structures of 1:1 co-crystals formed by p-$C_6H_4Me_2$ with p-$C_6F_4Br_2$ and p-$C_6F_4I_2$ are isomorphous. The solid-state structure are dominated by halogen bonding, with the I derivative forming the more common η_2 bonding while for the Br derivative the less common η_6 bonding is observed. Likewise, the co-crystal formed by C_6F_5I exhibits η_2 bonding but with only one iodine atom available in C_6F_5I, two molecules are required to enable halogen bonding to both sides of the aromatic ring of p-$C_6H_4Me_2$ leading to a 1:2 co-crystal. For C_6F_5I, the relatively large molecular dipole leads to a single solid-state phase with antiferroelectric ordering. However, for p-$C_6H_4Me_2$:C_6F_5Br, the balance of non-covalent interactions still leads to antiferroelectric ordering but with the molecules now arranged in *columns*.

For the columnar adducts, the non-covalent interactions can lead to either "staggered" or "eclipsed" arrangements with respect to the alignment of the C–X and C–Me bonds (with eclipsed forms favoured at lower temperatures); hence the variable phase behaviour seen in these derivatives. The weaker molecular dipole in C_6F_5Cl is insufficient to cause antiferroelectric ordering in p-$C_6H_4Me_2$:C_6F_5Cl, with disorder of the orientation of the C_6F_5Cl molecule being observed. A similar crystal structure was observed for one of the phases of p-$C_6H_4Me_2$:p-$C_6F_4Cl_2$ showing that one can indeed replace C_6F_5Cl with p-$C_6F_4Cl_2$ isostructurally. In contrast to the parent p-$C_6H_4Me_2$:C_6F_6 adduct, C_6F_5Cl, p-$C_6F_4Cl_2$, and C_6F_5Br adducts all exhibited phases with a slipped-disc arrangement for the columns of molecules, which is especially pronounced in the Br derivative due to steric effects.

In summary, this study provides valuable experimental data which will aid the development of crystal structure prediction (CSP) models and machine learning approaches. However, indexing of the powder diffraction pattern of "phase III" of p-$C_6H_4Me_2$:p-$C_6F_4Cl_2$ proved intractable, which throws open a challenge to our crystal-structure prediction colleagues.

Author contributions

The manuscript was written through contributions of all authors. All living authors have given approval to the final version of the manuscript.

Conflicts of interest

There are no conflicts to declare.

Data availability

Additional experimental details, crystallographic tables, additional supporting figures, and CIF files including the unindexed PXRD patterns are supplied in the supplementary information (SI).

Supplementary information is available. See DOI: https://doi.org/10.1039/d5ce00989h.

CCDC 2483307–2483317 (p-$C_6H_4Me_2$:C_6F_5Cl (in phases I and II), p-$C_6H_4Me_2$:p-$C_6F_4Cl_2$ (in phases I, II, and IV), p-$C_6H_4Me_2$:C_6F_5Br, p-$C_6H_4Me_2$:p-$C_6F_4Br_2$, p-$C_6H_4Me_2$:$(C_6F_5I)_2$, and p-$C_6H_4Me_2$:p-$C_6F_4I_2$, plus C_6H_6:p-$C_6F_4I_2$) contains the supplementary crystallographic data for this paper.[46a–k]

References

1 J. Maddox, *Nature*, 1988, **335**, 201.
2 (*a*) J. P. M. Lommerse, W. D. S. Motherwell, H. L. Ammon, J. D. Dunitz, A. Gavezzotti, D. W. M. Hofmann, F. J. J. Leusen, W. T. M. Mooij, S. L. Price and B. Schweizer, *et al.*, *Acta Crystallogr., Sect. B: Struct. Sci.*, 2000, **56**, 697–714; (*b*) A. M. Reilly, R. I. Cooper, C. S. Adjiman, S. Bhattacharya, A. D. Boese, J. G. Brandenburg, P. J. Bygrave, R. Bylsma, J. E. Campbell and R. Car, *et al.*, *Acta Crystallogr., Sect. B: Struct. Sci., Cryst. Eng. Mater.*, 2016, **72**, 439–459; (*c*) L. Hunnisett, J. Cole and G. Sadiq, *Acta Crystallogr., Sect. A: Found. Adv.*, 2022, **78**, a136; (*d*) L. Hunnisett, J. Nyman, N. Francia, G. Sadiq, I. Sugden, S. Reutzel-Edens and J. Cole, *Acta Crystallogr., Sect. A: Found. Adv.*, 2023, **79**, C160.
3 J. Nyman and G. M. Day, *CrystEngComm*, 2015, **17**, 5154–5165.
4 S. Erbas-Cakmak, D. A. Leigh, C. T. McTernan and A. L. Nussbaumer, *Chem. Rev.*, 2015, **115**, 10081–10206.
5 M. J. Webber and R. Langer, *Chem. Soc. Rev.*, 2017, **46**, 6600–6620.
6 K. Nakao, Y. Kamakura, M. Fujiwara, T. Shimizu, Y. Yoshida, H. Kitagawa, H. Yoshikawa, Y. Kitagawa and D. Tanaka, *Cryst. Growth Des.*, 2022, **22**, 26–31.

7 X. Pang, H. Wang, W. Wang and W. J. Jin, *Cryst. Growth Des.*, 2015, **15**, 4938–4945.

8 G. R. Desiraju, P. S. Ho, L. Kloo, A. C. Legon, R. Marquardt, P. Metrangolo, P. Politzer, G. Resnati and K. Rissanen, *Pure Appl. Chem.*, 2013, **85**, 1711–1713.

9 C. A. Hunter and J. K. M. Sanders, *J. Am. Chem. Soc.*, 1990, **112**, 5525–5534.

10 C. R. Patrick and G. S. Prosser, *Nature*, 1960, **187**, 1021.

11 B. J. J. Timmer and T. J. Mooibroek, *J. Chem. Educ.*, 2021, **98**, 540–545.

12 J. H. Williams, *Acc. Chem. Res.*, 1993, **26**, 593–598.

13 T. Dahl, *Acta Chem. Scand.*, 1994, **48**, 95–106.

14 C. R. Martinez and B. L. Iverson, *Chem. Sci.*, 2012, **3**, 2191–2201.

15 J. H. Williams, J. K. Cockcroft and A. N. Fitch, *Angew. Chem., Int. Ed. Engl.*, 1992, **31**, 1655–1657.

16 J. K. Cockcroft, A. Rosu-Finsen, A. N. Fitch and J. H. Williams, *CrystEngComm*, 2018, **20**, 6677–6682.

17 K. Carter-Fenk and J. M. Herbert, *Chem. Sci.*, 2020, **11**, 6758–6765.

18 J. Henrichsmeyer, M. Thelen, M. Bröckel, M. Fadel, S. Behnle, M. Sekkal-Rahal and R. F. Fink, *ChemPhysChem*, 2023, **24**, e202300097.

19 T. Dahl, *Acta Chem. Scand., Ser. A*, 1988, **42**, 1–7.

20 J. K. Cockcroft, R. E. Ghosh, J. J. Shephard, A. Singh and J. H. Williams, *CrystEngComm*, 2017, **19**, 1019–1023.

21 J. K. Cockcroft, J. G. Y. Li and J. H. Williams, *CrystEngComm*, 2019, **21**, 5578–5585.

22 S. Tsuzuki, T. Uchimaru and M. Mikami, *J. Phys. Chem. A*, 2006, **110**, 2027–2033.

23 A. P. West, Jr., S. Mecozzi and D. A. Dougherty, *J. Phys. Org. Chem.*, 1997, **10**, 347–350.

24 A. F. Tillack and B. H. Robinson, *J. Phys. Chem. B*, 2017, **121**, 6184–6188.

25 J. Řezáč, K. E. Riley and Pavel Hobza, *J. Chem. Theory Comput.*, 2012, **8**, 4285–4292.

26 S. E. Wheeler, *J. Am. Chem. Soc.*, 2011, **133**, 10262–10274.

27 J. C. Bear, R. E. Ghosh and J. K. Cockcroft, *Cryst. Growth Des.*, 2024, **24**, 3021–3029.

28 J. C. Bear, N. Terzoudis and J. K. Cockcroft, *IUCrJ*, 2023, **10**, 720–728.

29 *Handbook of Chemistry and Physics*, ed. D. R. Lide, CRC Press, London, 85th edn, 2004-5, ch. 3–74.

30 S. Konar, C. L. Hobday, C. L. Bull, N. P. Funnell, Q. F. Chan, A. Fong, N. Atceken and C. R. Pulham, *Cryst. Growth Des.*, 2022, **22**, 3862–3869.

31 J. C. Bear, A. Rosu-Finsen and J. K. Cockcroft, *CrystEngComm*, 2025, **27**, 1386–1391.

32 J. C. Bear and J. K. Cockcroft, *Chem. – Eur. J.*, 2024, **30**, e202402867.

33 S. d'Agostino, F. Spinelli, P. Taddei, B. Ventura and F. Grepioni, *Cryst. Growth Des.*, 2019, **19**, 336–346.

34 S. J. Kruse, L. R. MacGillivray and T. Z. Forbes, *Cryst. Growth Des.*, 2023, **23**, 3357–3366.

35 H. J. Frohn, S. Görg, G. Henkel and M. Läge, *Z. Anorg. Allg. Chem.*, 1995, **621**, 1251–1256.

36 M. Bujak, H.-G. Stammler and N. W. Mitzel, *Cryst. Growth Des.*, 2020, **20**, 3217–3223.

37 S. L. Chaplot, G. J. McIntyre, A. Mierzejewski and G. S. Pawley, *Acta Crystallogr., Sect. B*, 1981, **37**, 2210–2214.

38 S. Y. Oh, C. W. Nickels, F. Garcia, W. Jones and T. Friščić, *CrystEngComm*, 2012, **14**, 6110–6114.

39 S. J. Ang, A. M. Mak, M. B. Sullivan and M. W. Wong, *Phys. Chem. Chem. Phys.*, 2018, **20**, 8685–8694.

40 J. Vainauskas, *et al.*, *Chem. Sci.*, 2023, **14**, 13031–13041.

41 X. Pang, H. Wang, X. R. Zhao and W. J. Jin, *CrystEngComm*, 2013, **15**, 2722–2730.

42 L. Li, H. Wang, W. Wang and W. J. Jin, *CrystEngComm*, 2017, **19**, 5058–5067.

43 Q. J. Shen, H. Q. Wei, W. S. Zhou, H. L. Sun and W. J. Jin, *CrystEngComm*, 2012, **14**, 1010–1015.

44 Q. J. Shen, X. Pang, X. R. Zhao, H. Y. Gao, H. L. Sun and W. J. Jin, *CrystEngComm*, 2012, **14**, 5027–5034.

45 M. K. Corpinot and D.-K. Bučar, *Cryst. Growth Des.*, 2019, **19**, 1426–1453.

46 (*a*) CCDC 2483307: Experimental Crystal Structure Determination, 2025, DOI: 10.5517/ccdc.csd.cc2pc2pv; (*b*) CCDC 2483308: Experimental Crystal Structure Determination, 2025, DOI: 10.5517/ccdc.csd.cc2pc2qw; (*c*) CCDC 2483309: Experimental Crystal Structure Determination, 2025, DOI: 10.5517/ccdc.csd.cc2pc2rx; (*d*) CCDC 2483310: Experimental Crystal Structure Determination, 2025, DOI: 10.5517/ccdc.csd.cc2pc2sy; (*e*) CCDC 2483311: Experimental Crystal Structure Determination, 2025, DOI: 10.5517/ccdc.csd.cc2pc2tz; (*f*) CCDC 2483312: Experimental Crystal Structure Determination, 2025, DOI: 10.5517/ccdc.csd.cc2pc2v0; (*g*) CCDC 2483313: Experimental Crystal Structure Determination, 2025, DOI: 10.5517/ccdc.csd.cc2pc2w1; (*h*) CCDC 2483314: Experimental Crystal Structure Determination, 2025, DOI: 10.5517/ccdc.csd.cc2pc2x2; (*i*) CCDC 2483315: Experimental Crystal Structure Determination, 2025, DOI: 10.5517/ccdc.csd.cc2pc2y3; (*j*) CCDC 2483316: Experimental Crystal Structure Determination, 2025, DOI: 10.5517/ccdc.csd.cc2pc2z4; (*k*) CCDC 2483317: Experimental Crystal Structure Determination, 2025, DOI: 10.5517/ccdc.csd.cc2pc306.